Current-induced nonlinear magnetoelectric effects in strontium hexaferrite

I. V. Zavislyak, M. A. Popov, and G. Srinivasan

Phys. Rev. B **94**, 224419 — Published 19 December 2016

DOI: 10.1103/PhysRevB.94.224419

Current Induced Nonlinear Magnetoelectric effects in Strontium Hexaferrite

I.V. Zavislyak,[1] M.A. Popov,[1] and G. Srinivasan[2]

[1] Department of Radiophysics, Electronics and Computer Systems, Taras Shevchenko National University of Kyiv, Kyiv, 01601, Ukraine

[2]Physics Department, Oakland University, Rochester, MI 48309, USA

Abstract

We report on the first observation of nonlinear magnetoelectric effects at room temperature due to a DC current in the ferrimagnetic M-type strontium hexaferrite platelets. Utilizing microwave measurement techniques and data on the shift in magnetic mode frequencies, it was found that a DC current along the hexagonal *c*-axis resulted in a significant decrease in the saturation magnetization and an increase in the uniaxial magnetocrystalline anisotropy field. These changes in the magnetic order parameters were directly proportional to the square of applied electric field and were found to be much higher than variations due to Joule heating. A phenomenological theory that takes into account the current-induced magnetobielectric effects (MBE) is proposed. Expressions for coupling coefficients for MBE have been obtained and have been calculated from the variations in magnetic order parameters. The electric field E (or current) tuning of the magnetic modes in SrM reported here is orders of magnitude stronger than strain mediated E-tuning of magnetic resonance in hexaferrite-ferroelectric composites. The non-linear ME effects in the hexaferrite, therefore, open up an avenue for the realization of E-tunable broad-band microwave and millimeter wave ferrite signal processing devices such as resonators and filters.

1. Introduction

This report is on electric field control of magnetism in M-type hexagonal ferrite through nonlinear magnetoelectric interactions. There have been several reports in recent years on current/electric field control of ferroic order parameters in magnetic thin films and in composite structures. Efforts so far could be classified into two broad categories: (i) electric currents or spin currents in ferromagnetic films or composites [1-7] and (ii) influence of applied electric fields in single phase or composite multiferroics [8-16]. A rich variety of phenomena involving electron transport in ferromagnetic films or heterostructures were reported and were associated with the transfer of charge, spin-orbital moment or spin magnetic moment [17]. Examples include giant magnetoresistance, tunneling magnetoresistance, spin-Hall effect, and spin torque transfer that were successfully utilized for control of resistivity, magnetization reorientation and microwave generation [1-7]. Several useful applications including magnetic sensors, memory devices and spin-torque-nano-oscillators have also evolved from such studies [17].

Electric field control of magnetism is also well known in multiferroic materials with coexisting long range ordering of magnetic moments and electric dipoles. The magnetoelectric effect (ME) in such materials is defined as an induced magnetization (polarization) in an external electric (magnetic) field [8-12]. In a vast majority of single-phase multiferroics, however, the ME effect is rather weak even at low temperatures [8, 9, 18-22]. A strong ME coupling, could, however, be realized in a composite consisting of magnetostrictive and piezoelectric phases in which the ME effect is the result of a "product-property", i.e., the mechanical deformation due to magnetostriction resulting in dielectric polarization due to piezoelectric effects [10-14]. Studies so far have focused on thick films and thin film heterostructures and bonded bilayers of ferrites, manganites and metals/alloys for the ferromagnetic phase and several ferroelectrics including lead zirconate titanate and barium titanate [12]. A strong strain mediated ME coupling was reported in several of these

systems. Device applications for the ME effects in the composites include pico-Tesla magnetic sensors, gyrators, and voltage-tunable microwave ferrite signal processing devices [12-16].

Here we discuss the nature of electric field induced nonlinear ME interactions in the M-type strontium hexagonal ferrite $SrFe_{12}O_{19}$ (SrM) which is an n-type semiconductor. Linear ME effects are prohibited in M-type barium and strontium hexaferrites with collinear magnetic arrangement since the crystal symmetry contains spatial inversion element [18]. Such linear ME effects, however, are allowed in heavily doped M-type and Z-type hexaferrites in which the dopants replace Fe^{3+} and weakens the strength of exchange interactions, resulting in a spiral spin structure. Examples include Z-type $Sr_3Co_2Fe_{24}O_{41}$ and M-type $SrCo_2Ti_2Fe_8O_{19}$ and the application of an electric field to these ferrites induces a change in the magnetization [23-29]. The unit cell of strontium hexaferrite, the ferrimagnetic oxide considered in this study, consists of spinel and hexagonally packed blocks in which iron atoms are distributed among 5 different types of crystallographic sites (labeled 4f1, 4f2, 2a, 2b, 12k). Ferrimagnetic ordering of magnetic moments (with Fe at the 4f1 and 4f2 sites having their spins aligned anti-parallel to the rest of the Fe atoms) gives rise to a net ferromagnetic moment in the material. Although linear ME effect of the type *EH* (in the free energy) and nonlinear ME effects of the type *EHH* are forbidden in SrM, coupling of the type *HEE* (also called magnetobielectric interaction [18]) and higher order ME effects of the type *HHEE* are allowed [21, 30].

This report is on nonlinear ME interactions in SrM. An electric field *E* applied along the c-axis was found to result in a strong current induced non-linear ME interaction that manifests as variations in the magnetic order parameters (the ME phenomenon in this study could be described either as "*E*-induced" or as "*I*-induced" since the current is rather large in our semiconducting SrM platelets). We utilized microwave measurement techniques to estimate the changes in the magneto-crystalline anisotropy field and saturation

magnetization. The *I*-induced shift in the magnetic resonance frequency Δf_r in the multidomain depends only on the change in uniaxial anisotropy field. Data on Δf_r were used to estimate the change in the uniaxial anisotropy field H_a with *I*. Similar measurements were then carried out in the single domain (or saturated) state for estimating the change in the saturation magnetization M_0. Our data reveal a decrease in M_0 and an increase in H_a which scale linearly with the electric power density (or E^2). Although the influence of MBE effect on magnetic parameters is somewhat similar to thermal heating, we show that *I*-induced variations are much higher than expected changes due to Joule heating.

We have developed a phenomenological model for the non-linear ME effects from the free energy considerations. Expressions for variations in the magnetization and anisotropy field have been obtained in terms of the magneto-bielectric coupling coefficients. We estimated these coupling coefficients for SrM from the data on changes in the magnetic parameters versus electric power. The ME effects reported here are new and a theory for the mechanisms responsible for the current control of magnetism in SrM is yet to be developed. According to the density function theory SrM is a semiconductor with n-type conductivity with the bottom of conduction band consisting of electronic states of Fe ions [31]. Iron ions in the 12k-sites contribute substantially to the net ferromagnetic moment and Fe in 2b–sites to the uniaxial anisotropy constant K_u. Under a DC current, electrons from these sites are involved in the hopping-type conduction and the hopping occurs via intermediate oxygen atoms [32]. It is essential to model the influence of the conduction current along the *c*-axis on the magnetic exchange and spin-orbit coupling interactions and the resulting changes in the magnetic parameters

The results presented here are also of technological importance for tunable ferrite signal processing devices. Ferrites are the materials of choice for low-loss high frequency communication devices. Tuning of such devices has here-to-fore required the application of a large but variable external magnetic field that provides relatively slow tuning, utilizes

multi-watt levels of power which cannot be readily miniaturized or integrated with high frequency semiconductor (e.g. GaN or GaAs) devices. However, voltage tuning of ferrite-ferroelectric devices through mechanical strain coupling was demonstrated in recent years, but the tuning was rather small, on the order of 0.01% for hexaferrite-PZT [15,16]. The tuning of resonance modes reported here, however, is one to two orders of magnitude higher than strain mediated voltage tuning. The tuning under multi-domain state, in particular, will facilitate ferrite devices such as resonators and filters that do not require a bias magnetic field. As discussed later in Sec.3 one could potentially achieve GHz-tunability by decreasing the ferrite thickness and controlling the sample conductivity. It is therefore possible to realize miniature, multi-octave current-tunable ferrite devices enabling agile communication systems that can essentially provide rapid frequency hopping between RF bands.

In the sections to follow, we provide details on results of our studies on non-linear ME interactions in SrM and discuss the results in terms of a phenomenological model.

2. Experiment

2.1. Electrical characterization

The samples used in this study were single-crystals strontium hexaferrite of the stoichiometric composition $SrFe_{12}O_{19}$ grown by floating zone techniques. Samples were cut into thin platelets with the *c*-axis perpendicular to the plane. The specimens had lateral dimensions a×b = 2.0×1.5 mm^2 and thickness d=160 μm. Electrodes (1.5 μm thick Pt with 10 nm Ti underlayer) were deposited on the top and bottom surfaces by RF sputtering. The bottom surface of the sample was completely covered with Pt, whereas a 0.75 mm wide conducting stripe was formed in the middle of the top surface of the sample. The measurement cell (shown in Fig. 1) consisted of a copper plate with the sample bonded to it with a thin layer of an alloy. A small hole was drilled in the Cu-plate next to the sample and was used to connect a thin wire to the top electrode. Thus, under an applied voltage a

current was established along the c-axis, across the thickness of the ferrite. The bottom Cu-plate also served as a heat sink.

The SrM samples were first characterized in terms of electrical properties by measuring the current I as a function of applied voltage U and temperature T. Such data are essential for information on the nature of electrical conduction mechanism. The hexaferrite together with copper plate was placed inside a temperature controlled chamber and I vs U data as in

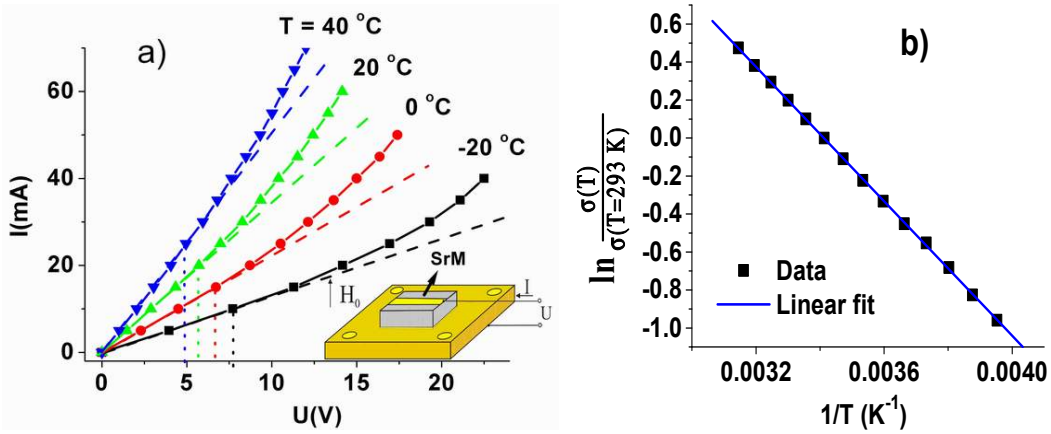

Fig. 1 a) Current I versus voltage U data as a function of temperature T for a c-plane platelet of single crystal strontium hexaferrite. The current is directed along the c-axis. Vertical dotted lines show the region of linear I vs. U behavior. Inset shows the measurement cell with the ferrite platelet with electrodes mounted on a Cu-flange. b) Normalized small-signal conductivity σ vs. inverse temperature data for the SrM platelet. The conductivity values were calculated from the linear regime of the data in (a)

Fig.1(a) were obtained for a series of temperatures. These data reveal a linear behavior for U in the range 0 to 7 V and then becomes nonlinear at higher voltages as expected for semiconductors. The conductivities σ were then calculated as a function of temperature from the linear regime of the data in Fig.1(a) and the results are shown in Fig.1(b). For $U >$ 7 V, however, σ is dependent on U. The data in Fig.1(b) were fitted to the relation $\sigma(T) = \sigma_0 e^{-q/kT}$ for hopping-type conduction [33]. We estimated an activation energy of $q =$ 0.153 ± 0.001 eV that is in agreement with reported results for barium hexaferrite, a closely-

related compound [32]. As described later in Sec.2.3, the data in Fig.1(b) were also used for determining the sample temperature under a current.

2.2 Magnetic resonance modes in multi-domain and single domain states

We first characterized the high frequency modes in the absence of a DC excitation current in order to establish the baseline resonance behavior. For these measurements, the Cu plate with the sample was placed at the open end of a waveguide in order to form a short (see Fig. 2a) and profiles of scattering matrix parameter S_{11} (reflection coefficient) vs frequency f were recorded and analyzed. The RF power was kept low, approximately 1 mW, to avoid any sample heating. The waveguide section with the sample was placed between the pole pieces of an electromagnet so that the bias field H_0 was directed perpendicularly to the sample plane and parallel to the hexaferrite *c*- axis.

The measurements were done using two scalar network analyzers, 37-53 GHz and 53-78 GHz frequency bands, and results on mode frequency f_r as a function of H_0 were then combined to a single plot shown in Fig.2(b). The data are for the sample in the multidomain (H_o below magnetic saturation) and single-domain (saturated) states. Several modes were observed in both states. The data in Fig.2 shows modes in the multi-domain state that ultimately evolve into (1,1) and (1,3) modes in the single domain state. Splitting of these (1,1) and (1,3) modes occur in both multi-domain and single domain states due to the shielding effect of the Pt-electrodes. Modes that originate from the sample volume enclosed between the top and bottom electrodes have a higher frequency than the modes from the rest of the sample and are designated as $(1,1)'$ and $(1,3)'$. Models for f_r vs. H_o in the multi-domain state are rather complicated and sensitive to the actual configuration of domain structure [34].

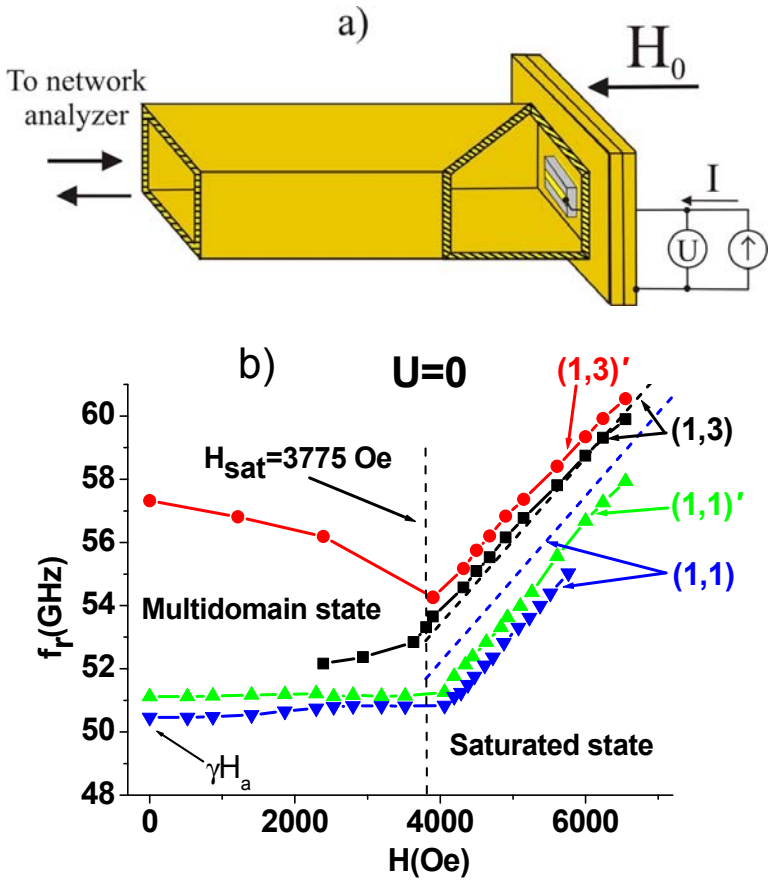

Fig. 2 a) Diagram showing the experimental set-up for measurements on magnetic resonance modes in SrM. b) Resonance frequency f_r vs. bias magnetic field H_0 dependence for magnetostatic modes of SrM in multidomain and saturated states. Symbols represent data points, solid lines are guides to the eye, and dashed lines are theoretical estimates.

The mode with the lowest frequency in the multi-domain state is the domain resonance with the frequency f_r given by [34]

$$f_r(H_0 = 0) = \gamma(H_a - 4\pi M \cdot N_{zz}^{eff}) \,, \qquad (1)$$

where the gyromagnetic ratio γ=2.66 MHz/Oe [35], $H_a = 2K_u / M_0$ is the uniaxial anisotropy field and K_u is an anisotropy energy constant, and N_{zz}^{eff} is the effective demagnetization coefficient [36]. Under $H_0 = 0$ the sample with uniaxial anisotropy along c-axis splits into oppositely magnetized stripe domains of equal volume so that $4\pi M \sim 0$. Under these assumptions, the demagnetization term in Eq.(1) is zero and may be neglected.

We could, therefore, use data on f_r for H_0 =0 to calculate the value of H_a and its variation with current I. In the absence of an excitation current, we estimated $H_a \approx 18.9$ kOe from the data in Fig.2(b) and is in good agreement with reported values [37].

In the (single domain) saturated state, magnetostatic forward volume waves are excited in the sample. The dispersion equation for the modes in a ferrite with one side metallized is given by [38]

$$|k|d = \frac{1}{\sqrt{-\mu}} arctg\left(\frac{1}{\sqrt{-\mu}}\right), \qquad \mu = \frac{f^2 - f_H(f_H + f_M)}{f^2 - f_H^2}. \tag{2}$$

Here k is a transverse wavenumber, μ is the diagonal element of the rf permeability tensor, $f_H = \gamma(H_i + H_a)$, $f_M = \gamma 4\pi M_0$, and $H_i = H_0 - N_{zz} 4\pi M_0$ (where $4\pi M_0$ is a saturation magnetization and N_{zz} is the demagnetizing factor along c-axis). For our sample we estimated N_{zz} = 0.818 [39]. Mode wavenumber for a rectangular straight-edge resonator is given by $k^{\{nm\}} = \pi\sqrt{(n/a)^2 + (m/b)^2}$, $n,m = 1,2,3...$ and the corresponding mode is then designated by the indices (n,m) [38]. The mode frequencies in the saturated region of Fig.2(b) with linear f_r vs. H_o dependence correspond to the two lowest frequency forward volume modes which were identified as (1,1) and (1,3) modes. Estimated frequencies for (1,1) and (1,3) modes are shown for comparison and the minor discrepancy between theory and experimental values for the (1,1) mode could be attributed to the retardation effect associated with metallized ferrites [38].

Data in Fig.2 also indicates splitting of the (1,1) and (1,3) modes into doublets labeled (1,1) - (1,1)′ and (1,3) - (1,3)′, respectively, with the frequency gap between the doublets much smaller than the gap between the two primary modes. We attribute the presence of the doublets to non-uniform metallization of the sample leading to differences in the boundary conditions. It is well known that the top and bottom metallization strongly influence the frequencies of forward volume magnetostatic wave modes [40]. Moreover, double-sided

metallization leads to higher mode frequency. In the present case the sample has double-sided metallization only in the central part and has a single-sided metallization elsewhere. Hence, magnetostatic modes that are primarily localized in the center of the sample will differ in frequency from the modes localized away from the center.

Next we consider the variation in mode frequencies due to any change in the magnetic parameters in the single-domain state. For a specific value of wavenumber $k = k^{\{nm\}}$ we have $\mu = \mu^{\{nm\}}$ = *constant* from Eq.(2). Then after differentiating the expression for μ in Eq.(2) and equating $d\mu^{(mn)} = 0$, we get the following expression for the frequency shift

$$\frac{\Delta f^{\{nm\}}}{\gamma} = \left(\frac{f^2 + f_H^2}{2 f_H f} \Delta H_0 + \frac{f^2 + f_H^2}{2 f_H f} \Delta H_a + \frac{f_H (f^2 - f_H^2) - f_M N_{zz} (f^2 + f_H^2)}{f_M f_H f} \Delta (4\pi M_0) \right) \Bigg|_{f = f^{\{nm\}}},$$

where the right-hand side should be evaluated for a given mode frequency. Since for small ($k^{\{nm\}} d$) values $f^{\{nm\}} \approx f_H$ the above expression may be reduced to

$$\frac{\Delta f^{\{nm\}}}{\gamma} \approx \Delta H_0 + \Delta H_a - N_{zz} \Delta (4\pi M_0). \qquad (3)$$

It is clear from Eq.(3) that (i) changes in f_r are directly proportional to the sum of changes in M_o and H_a and, therefore, data on current-induced frequency shift may be used to estimate variations in these magnetic parameters, and (ii) the frequency shift does not depend on frequency of a specific mode. Thus identical shift in frequency is expected for all lowest-order magnetostatic modes. For a specific mode and for constant bias field H_0, the frequency shift is due to changes in H_a and M_o.

The bias field required for the single domain state $H_0 = H_{sat}$ was determined by careful measurement of the mode frequency in the transition region between multi-domain and saturated states and was found to be $H_{sat}^{\exp}$ = 3775 Oe. One expects saturation to occur for $H_i = 0$ or $H_{sat} = 4\pi M_0 \cdot N_{zz}$. Substituting for $4\pi M_0$ = 4652 G [41] and N_{zz} = 0.818, we get H_{sat}^{theory} = 3805 Oe, in agreement with the experiment.

2.3 Effects of Joule Heating on Magnetic Parameters

In order to rule out the influence of Joule heating from the ME effects we wish to study, we measured the electrical resistance of the sample as a function of temperature in a separate experiment. Although the copper flange on which the SrM platelet is mounted acts as a heat sink for the heat generated under a current pulse, sample heating inevitably occurs and will lead to variation in the magnetic parameters and a shift in f_r. So it was necessary to investigate the current induced change in the sample temperature. We performed a detailed and systematic study to assess the extent of sample heating and its contribution to changes in M_0 and H_a. In order to avoid complications associated with temperature measurements using an external probe, we utilized electrical conductivity σ vs T data in Fig.1(b) to determine the sample temperature from measured σ-values.

Measurements on thermally induced effects were done using the following procedure. A DC current of preset magnitude was supplied to the sample for a prolonged period of ~10 min. Then at certain time intervals, varying from 5 s to 1 min, the current was switched off momentarily and sample resistance was measured using the same electrodes used for the current application. After 10 minutes the current was turned off and the sample resistance was measured at periodic intervals as the sample was cooled. The sample temperature was then determined from σ vs T data in Fig. 1(b). Figure 3 shows the sample temperature thus obtained as a function of time for currents up to a maximum of 70 mA. The sample temperature initially increases rapidly with time over the interval t= 0 to 100 s. The rate of increase in T with time over this interval ranges from 0.02 ^{0}C/s for I=50 mA to 0.04 ^{0}C/s for I = 70 mA. Then the rate of increase in T with t slows down and finally it levels off. Since we are primarily interested in the sample heating characteristics for the low t-region in Fig.3, we used excitation currents that are pulses of 1 s duration in our experiments as described in the following section. Figure 3 also shows the ΔT vs t profiles for the time interval t = 0-60 s. From the data in Fig.3 for t = 0-5 s, we estimated $\Delta T/\Delta t \approx$0.25 °C/s for I

= 70 mA. Therefore, for current pulses of 1 s duration, the temperature rise may not exceed 0.25 ^{0}C for the currents used in our experiments.

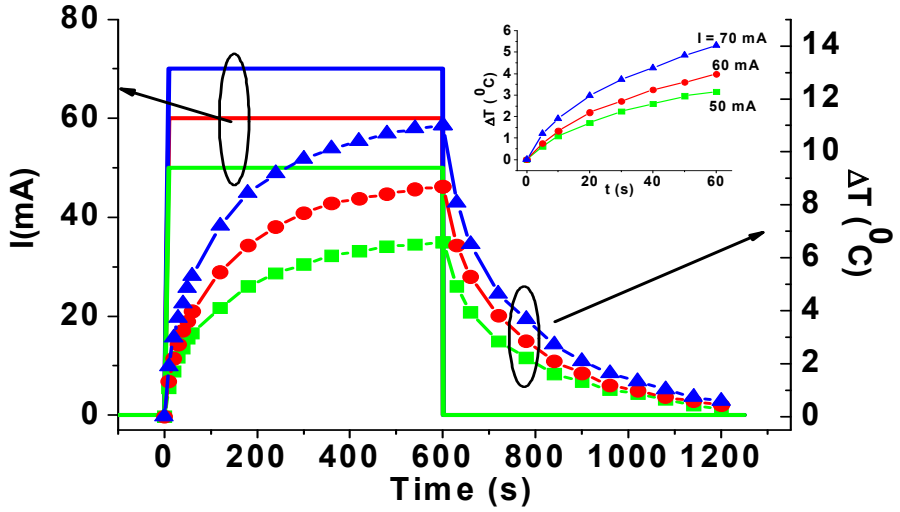

Fig. 3. Change in temperature ΔT of SrM as a function time t under a current pulse of duration 10 min and different amplitudes. The inset shows increase in sample temperature during the initial 1 min. Also shown is the ΔT vs t data when the current is switched off and the sample cooled down to room temperature.

Following the acquisition of the data in Fig.3, we estimated the anticipated change in f_r in the multidomain and single domain resonance due to the expected increase in sample temperature. Additional experiments, conducted in environmental chamber in the same temperature range, yielded an estimated upshift of Δf_r = 3.7 MHz for multi-domain resonance for 0.25°C increase in T that can only be attributed to an increase in H_a with increasing temperature (Eq.1). On the other hand, fractional decrease in the saturation magnetization with temperature $\frac{1}{\Delta T}\frac{\Delta(4\pi Mo)}{4\pi M}$ for SrM was reported to be -0.002/°C [42, 43]. Hence, for $4\pi M_0$ = 4652 G [41], we obtain $\Delta(4\pi Mo)/\Delta T \approx$ -9 G/°C corresponding to $\Delta f_r = -\gamma \cdot \Delta 4\pi Mo =$ 6 MHz for 0.25 C increase in T. Summarizing, the potential contribution of Joule heating to frequency shift during 1s, 70 mA current-pulse is estimated to be $\Delta f_r^{thermal} \approx 4$ MHz for the multidomain state measurements and $\Delta f_r^{thermal} \approx 9.7$ MHz for

the saturated-state (Eq. 3). As discussed in the section to follow, the frequency shifts in f_r due to non-linear ME interactions are at least an order of magnitude higher than the variations originating from Joule heating. One could, therefore, rule out any significant contribution from the Joule heating to variation in the magnetic parameters and a shift in the magnetic mode frequencies.

2.4 Microwave Measurements on Current Induced ME effects

Next we discuss our investigations on the current induced nonlinear ME effects. During the measurements, short current pulses were applied and the resonance frequency was measured as a function of current (input power). The measurements involved applying rectangular current pulses of short duration. The pulse width was selected short enough to limit the influence of Joule heating as discussed in Sec.2.3. Once the current stabilized we recorded the resonance profiles.

One may utilize profiles of either S_{11} vs f at constant bias magnetic field or S_{11} vs H at constant f for such measurements. For multi-domain resonance we are primarily interested in the S_{11} *vs* f profiles due to the fact that it is possible to readily estimate H_a and its current variation directly from the resonance frequency and using Eq.(1). For single-domain resonance both types of profiles could be used to determine the resonance field and its shift under a current pulse. Resonance profiles under zero current and upon the application of a current pulse are shown in Fig. 4. Profiles in Fig.4(a) are for the sample in the multidomain state whereas Fig.4(b) shows similar results for forward volume waves in the sample magnetized to saturation. Fig.4(c) shows a representative example for S_{11} vs H_0 profiles measured at constant f. Such profiles are useful since they are less susceptible to broadening due to unwanted electrodynamic ripples that appear in transmission characteristic when using frequency sweeps. However, in the multi-domain state f_r has a weak dependence on H_0 as seen in the data of Fig. 2(b), and S_{11} vs H_0 are not appropriate for this specific case.

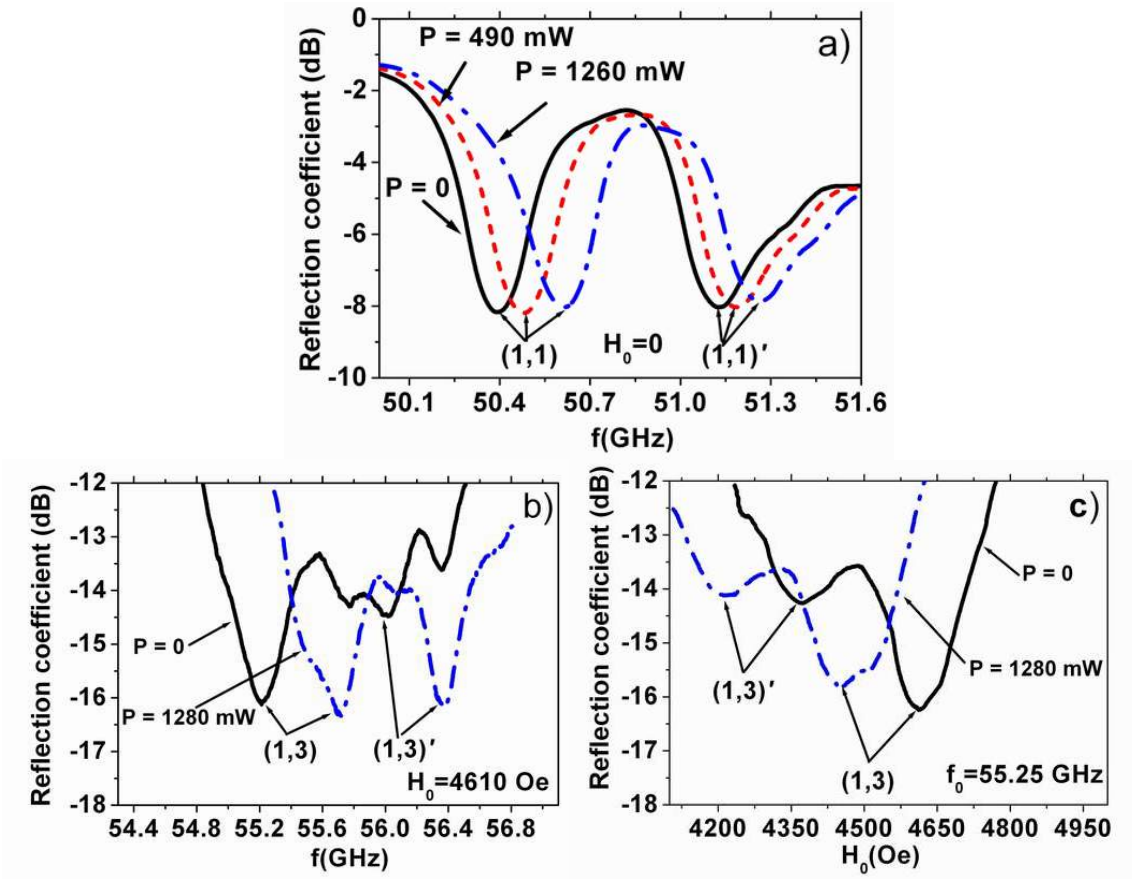

Fig. 4. Reflection coefficient vs. f data as a function of electric power applied to the sample (a) in the multidomain state (H_o=0) and (b) in the single domain state. (c) Reflection coefficient vs. H_o for the single domain state. The current pulses were of 1 s duration, ~ <10 ms rise/fall time and 10-70 mA amplitude.

Therefore S_{11} vs f profiles are preferred in this study. Finally, such profiles also clearly demonstrate the tunable broad-band ferrite device aspect of the phenomenon discussed here.

Data on S_{11} *vs* f profiles were acquired for frequency increments of 1 MHz. The mode frequency f_r and the shift Δf_r were determined from the frequency that corresponds to the minimum in the reflected power. The error in S_{11} for our network analyzers was on the order of ΔS_{11}=0.03 dB, corresponding to an absolute error $\Delta f \approx$20 MHz in the frequency measurements. The relative error in the mode frequency was much lower than the absolute error and is on the order of 3 to 4 MHz. In the multidomain state two resonance modes are

seen in Fig.4(a). We identify the modes with the labels (1,1) and (1,1)′ since they evolve into these modes (as shown in the data of Fig.2) in the saturated state. Both the multi-domain and single domain state have a resonance mode that is higher for 2-sided metalized ferrite then 1-sided metalized ferrite [40,44] which allowed us to label the individual modes in Figs. 2 and 4. The two modes in Fig.4(a) are separated by 750 MHz for zero-current. Both modes showed a significant increase in the resonance frequency when a current was applied to the sample. Figure 5 shows the increase in frequency Δf_r vs electric power P. The frequency shift for the low-frequency (1,1) multidomain mode is shown since Eq. (1) holds true for this mode and the data is sufficient for our analysis. A shift of identical magnitude was measured for the high frequency (1,1)′ mode.

Resonance profiles in Fig. 4(b) are for the modes (1,3) and (1,3)′ for the sample in the single domain state. The resonances in the single domain state are rather broad in comparison to the multidomain case even though one would anticipate a broader resonance absorption in the multi-domain case. In thin platelets of ferrites with uniaxial anisotropy, such as SrM, the stripe domains with antiparallel magnetization have equal volumes and are separated by Bloch-type domain walls (DW). There are two types of eigen-modes in the multi-domain state; one is excited by ac magnetic fields parallel to the domain walls and the other by ac field perpendicular to DW. The mode in our case is the latter one, for which magnetization oscillations are continuous across the DW, and hence no high-frequency demagnetizing field appears on DW. Thus there are no new two- and three-magnon relaxation mechanisms expected in the multi-domain resonance and this mode may not have a higher linewidth than for the saturated single-domain state. The broad resonance absorptions in the saturated state in the present case may in part be due to a resonance frequency ~ 10% higher than the multi=domain resonance and forward volume wave nature of the excitations. This observation needs further investigation.

We also observed splitting of the modes in Fig.4(b), i.,e ripples, in otherwise smooth S_{11} vs f characteristics. The ripples are distortions caused by electrodynamic perturbation of waveguide modes due to the presence of sample. The nature of these ripples are dependent on the sample geometry and location in the waveguide, but their frequency did not change with H or I. Figure 5 shows the shift Δf_r in the frequency of (1,3) mode as a function of the electric power in the saturated state. Values of Δf_r were corrected for increase in T due to Joule heating as discussed in Sec.2.3. In the saturated state, both (1,3) and (1,3)′ modes showed the same frequency shift. We made measurements of Δf_r vs p for six different static magnetic field values in the range H_0 = 4-6.5 kOe and found a very weak dependence of Δf_r on H_0 in agreement with the theoretical predictions [Eq. (3)].

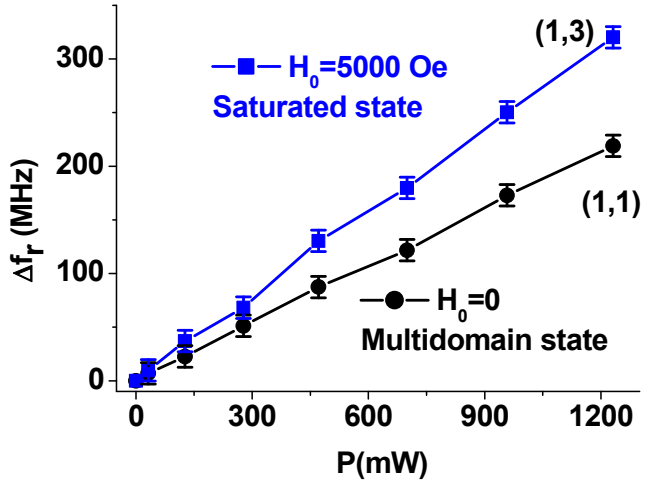

Fig. 5. Frequency shift for magnetic resonance modes Δf_r as a function of applied power P in multidomain and single domain states of SrM.

The data in Fig. 5 show a much higher current-induced shift in f_r in the single domain state than for the multi-domain resonance. In the multidomain case any change in H_a influences the mode frequency, whereas in the saturated state changes in both $4\pi M_0$ and H_a contribute to the frequency shift. The I (or E-) induced shifts in f_r in Fig.5 are the highest reported for any hexagonal ferrite. The maximum frequency shifts in Fig.5, ~ 220 MHz in the multidomain state and ~320 MHz in the saturated state for E ~ 1 kV/cm, are two orders

of magnitude higher than shifts of ~ 0.6 MHz in FMR for E = 1 kV/cm in BaM-PZT composites due to strain mediated coupling [16, 23].

Next, we utilized Δf_r *vs* P the data in Fig.5 to estimate the changes in the anisotropy field and magnetization with the electric power density $p = P/V$, where V is the sample volume. First, the data for the multi-domain state and Eq.(2) were used to estimate the variation in ΔH_a. Then we obtained $\Delta(4\pi M_0)$ vs. p using Eq.(3), the frequency shift data in the saturated state, and previously estimated ΔH_a values. Figure 6 shows p-dependence of variations in $4\pi M_o$ and H_a. Since there is a linear relationship between the mode frequency and uniaxial magnetic field and magnetization, [Eqs. (1) and (3)] the uncertainty in Δf_r corresponds uncertainty of 8 Oe in the anisotropy field (or the magnetization) values.

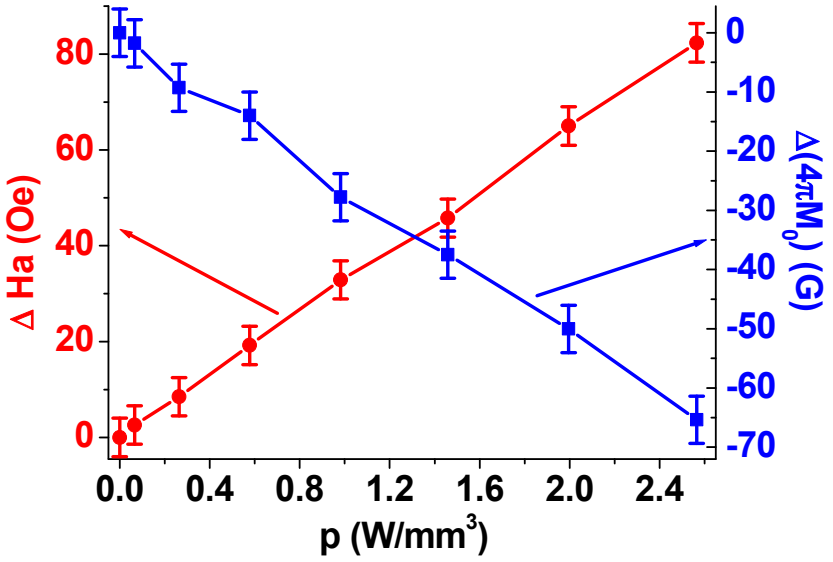

Fig. 6. Current induced variation in the uniaxial anisotropy field and saturation magnetization as a function of electric power density. Error bars show measurement uncertainty due to the Joule heating.

This accuracy sets the size of error bars in Figs. 5 and Fig. 6. The anisotropy field in Fig.6 is found to increase with p, whereas M_o decreases with increasing electric power. Both parameters show linear dependence on the electric power density (or E^2). Since the uniaxial anisotropy field $H_a = 2K_u / M_0$, changes in both K_u and M_o will ultimately determine the net

variation in H_a. The variation in the anisotropy field is given by $\Delta H_a = \frac{\partial H_a}{\partial K_u}\Delta K_u + \frac{\partial H_a}{\partial M_0}\Delta M_0$ and

$$\frac{\Delta H_a}{H_a} = \left(\frac{\Delta K_u}{K_u} - \frac{\Delta M_0}{M_0}\right). \qquad (4)$$

Although both K_u and M_o are expected to decreasing with increasing p, one infers from the results in Fig.6 that $\left|\Delta K_u / K_u\right| < \left|\Delta M_0 / M_0\right|$, so that $\Delta H_a / H_a > 0$.

3. Discussion

The presence of free charge carriers in both spinel and hexagonal ferrites is known to lead to such effects as eddy current losses, magneto-plasmon-polariton formation and propagation, and magnon-electron relaxation processes [45]. Yet, none of these can be the cause of the observed modification of magnetic parameters. The first-principles band structure calculations for SrM using the density function theory show that the electronic structure for this compound is a semiconductor with a direct energy gap of about 0.63 eV and n-type conductivity along hexagonal c-axis [31]. Magnetic structure calculations predict that the most stable magnetic structure of the ferrite is ferrimagnet with Fe in the 4f1 and 4f2 sites having the magnetic moments anti-parallel to the rest of the Fe.

The electrical conductivity in SrM is the result of electron hopping between Fe^{3+} and Fe^{2+} ("valence exchange") [32,46], presumably via intermediate oxygen atoms [31]. In stoichiometric SrM the unit cell is charge balanced and hence the hopping process is impossible. But in ferrites with excess iron or oxygen deficiency, charge imbalance promotes Fe^{2+} formation and leads to hopping type electrical conduction [47].

Next we speculate on the possible causes for the current induced changes in the magnetic order parameters. From the results presented here it is clear that the current conduction process has a significant impact on both the magnetization and anisotropy. In

this respect it is similar to effects of Joule heating. The electron hopping, however, is much faster than the heating process and this allowed us to separate the two contributions. As seen in the data of Fig.6, the observed ME effects are proportional to the power density $p = P/V = \sigma_{||} E^2 = \sigma_{||} U^2 / d^2$. It is also clear from *I vs U* data in Fig.1 that σ is independent of the applied voltage *U* only for *U* ~ 0-7 V and, therefore, changes in M_0 and H_a are directly proportional to E^2 for low input power. However, nonlinear *I* vs *U* behavior for *U* > 7 V need to be carefully considered for an understanding of the results in Fig.6 and for modeling efforts of the non-linear ME effects in materials with semiconductor type of conductivity. From the expression for *p* we expect the strength of ME interactions to increase linearly with σ and decrease with increasing *d*. Moreover, a decrease in sample volume will also result in an increase in the sample surface area- to-volume ratio and an efficient transfer of heat generated due to Joule heating to the Cu holder. Thus as the sample size decreases one anticipates weakening of Joule heating related effects on magnetic parameters. Studies on micro- and nano-dots of hexaferrites are of interest in this regard.

Next we compare the *E*- (or *I*-) tuning of resonance modes in SrM with magnetic and *E*-tuning of resonances in other microwave ferrites and yttrium iron garnet (YIG). Ferrite and YIG devices based on magnetic modes or FMR in general are tuned with a magnetic field produced by an electromagnet or a solenoid. Broad-band tuning *H*-tuning was demonstrated for devices such as resonators and filters [15]. Another tuning procedure involves application of a dc voltage to a ferrite/YIG-ferroelectric composite. Such composites are multiferroics and show coupling between electric and magnetic subsystems that is mediated by mechanical strain and occurs through. magnetostriction in the ferrite and converse piezoelectric effect in the ferroelectric. Thus one can control electromagnetic properties of a composite with *E* and/or *H*. Under the application of an electric field, the ME effect in the composite can be observed in the form of a shift in ferromagnetic resonance (FMR) profile for the ferrite. Voltage tuning of several YIG-PZT and ferrite-PZT devices

including resonators, band-pass filters, phase shifters, and delay lines were reported [15]. However, *E*- tuning is rather weak for hexaferrite-PZT due to low magnetostriction of the former and was on the order of 0.6 MHz of the central frequency for a BaM-PZT resonator for E = 1 k V/cm [16]. In the present study, the tuning is on the order of 250-300 MHz for E = 1 kV/cm (Figs. 4 and 5) and is two orders of magnitude higher than for the strain mediated tuning. Thus this report on nonlinear ME interaction mediated tuning of FMR/magnetic modes is of importance for a new family of broad-band E-tunable hexaferrites devices.

3.1 A model for the non-linear ME effects

Next we consider a model for the observed effects. The free energy density for SrM (in CGS units) can be expressed as:

$$G = G_0 + G_{ME} \tag{5}$$

Here G_0 is the free energy of the magnetic system in the absence of electric field and includes Zeeman energy and energy associated with to exchange interactions, dipole-dipole interaction, and spin-orbital coupling. G_{ME} is the magnetoelectric energy that is traditionally written as a series with ascending powers of electric and magnetic fields [18,21] and should be consistent with the crystal symmetry of a given material. Specifically, for M-type hexaferrites with collinear magnetic arrangement both linear magnetoelectric term $\alpha_{ij}E_iB_j$ and electro-bimagnetic $\beta_{ijk}E_iB_jB_k$ effects are prohibited [18] since its crystal structure has the center of inversion. For the same reason, all higher order terms may only contain electric field in even power. We use B instead of H for magnetic field since the former is more appropriate for the magnetically saturated materials with non-zero spontaneous magnetization [18,21]. We therefore express G_{ME} as

$$G_{ME} = -\frac{1}{4\pi}\left(\gamma_{ijk}B_iE_jE_k + \frac{4\pi}{M_0^2}\delta_{ijkl}E_iE_jM_kM_l\right). \tag{6}$$

Here γ_{ijk} denotes the coefficient of the magneto-bielectric effect (MBE) and δ_{ijkl} is the coefficient for the second order magnetoelectric term contributing to magnetocrystalline anisotropy constant [30]. Note that ME terms in Eq.(6) are quadratic in *E*. That is in agreement with our results in Fig.6 where all measured changes in magnetic parameters are found to be linearly proportional to electric power density.

Consider first the magneto-bielectric term in G_{ME} given by

$$G_{ME}^{MBE} = -\frac{1}{4\pi}\gamma_{ijk} B_i E_j E_k .$$

The change in the static magnetization due to MBE is given by

$$\Delta M_i^{MBE} = -\frac{\partial G_{ME}^{MBE}}{\partial B_i} = \frac{1}{4\pi}\gamma_{ijk} E_j E_k . \qquad (7)$$

The terms γ_{ijk} in the magneto-bielectric tensor are determined by the symmetry properties of the crystal structure of SrM. According to the Neumann principle, the γ_{ijk} tensor must be invariant with respect to all transformations connected with the symmetry operation of the specific magnetic point group which is $6/mm'm'$ in the case of M-type hexaferrites [49]. One needs to consider the γ_{ijk} tensor with all of the 27 coefficients present and then impose the condition that this tensor has to be invariant under all the transformations. Each symmetry operation leads to 27 equations (one for each tensor component) and in turn provides equations relating the tensor coefficients. These equations are then solved to obtain the nonzero tensor components. The magneto-bielectric tensor, however, has essentially the same form as the piezomagnetic tensor Λ_{ijk} for this point group [18]. Using the Voigt notation for the indices for the tensor components $\gamma_{ijk} = \gamma_{il}$ with *l* represented by 1 for *j,k* =11; 2 = 22; 3 =33; 4 =23=32; 5=31=13; 6=12 =21, one arrives at the following coefficients for the tensor [50].

$$\gamma_{il} = \begin{pmatrix} 0 & 0 & 0 & 0 & \gamma_{15} & 0 \\ 0 & 0 & 0 & \gamma_{15} & 0 & 0 \\ \gamma_{31} & \gamma_{31} & \gamma_{33} & 0 & 0 & 0 \end{pmatrix}$$

For the MBE tensor γ_{ijk} tensor we obtained the following non-zero coefficients $\gamma_{131} = \gamma_{232} = \gamma_{113} = \gamma_{223}$, $\gamma_{311} = \gamma_{322}$, γ_{333}. Hence, the change in magnetization along the six-fold symmetry axis (denoted here with index 3) is

$$4\pi\Delta M_3^{MBE}(\bar{E}) = \gamma_{311}E_\perp^2 + \gamma_{333}E_\parallel^2 \qquad 8(a)$$

where $E_\perp$ and $E_\parallel$ denote static electric field components perpendicular and parallel to the hexaferrite c-axis. Equation 8(a) implies anisotropic nature of MBE in SrM with the change in the static magnetization dependent on the direction of electric field. Substituting for *E* in Eq.8(a) by $E_i = \rho_{ij} j_j$, where $\rho_{ij} = (\sigma_{ij})^{-1}$ is the anisotropic resistivity tensor [32], we get

$$4\pi\Delta M_3^{MBE}(\bar{j}) = \gamma_{311}\rho_\perp^2 j_\perp^2 + \gamma_{333}\rho_\parallel^2 j_\parallel^2 . \qquad 8(b)$$

Expression 8(b) does not take into account the dependence of the resistivity tensor components on the electric field and is valid only for materials with ohmic or quasi-ohmic conductivity. In other cases, e.g. for semiconductors in nonlinear regime, dependence of ρ_{ij} on *E* should be explicitly taken into account.

The input electric power is given by $P = UI$ with $U = \int_L \bar{E} d\bar{l}$ and $I = \int_S \bar{j} d\bar{S}$. In our case $\bar{j} = (0,0,j_\parallel)$ and therefore $P = \rho_\parallel j_\parallel^2 V$, and sample volume $V = abd$ (a and b are the lateral dimensions of the sample). Thus $\rho_\parallel j_\parallel^2 = P/V$ and the magnetization change $4\pi\Delta M_3$ is quadratic in electric field $\bar{E}$ and a linear function of electric power density *P/V*. The duality of magnetoelectric effect implies that besides electric field induced magnetization a magnetic field induced polarization should also exist. One obtains for the induced polarization $\Delta P_i^{MBE} = -\frac{\partial G_{ME}^{MBE}}{\partial E_i}$ and for $\bar{B} = (0,0,B_3)$, ΔP_i is given by

$$4\pi\Delta\bar{P}^{MBE}(\bar{E}) = 2\gamma_{311}B_3\bar{E}_\perp + 2\gamma_{333}B_3\bar{E}_\parallel . \qquad (9)$$

Thus the effect can be treated as a magnetic field induced modification of dielectric permittivity: $\varepsilon_{ij} = \varepsilon_{ij}^0 + \Delta\varepsilon_{ij}(\gamma_{mnp}, \overline{B})$ where the specific form of $\Delta\varepsilon_{ij}(\gamma_{mnp}, \overline{B})$ term depends on the crystallographic symmetry and direction of flux density vector. Using Eq. (8) and experimental data, one can estimate the value of magneto-bielectric coefficient γ_{333}. Our estimates provided γ_{333}=5.6·10^{-9} Gm^2/V^2 that corresponds to γ_{333}=5.1 cm/statV in CGS.

Electric field-induced modification of magnetocrystalline anisotropy is accounted for in a similar way by using the second term in Eq.(6). From symmetry considerations discussed above for the tensor γ, it can be shown that the tensor δ_{ijkl} has 21 non-zero coefficients (6 independent) for the $6/mm'm'$ point group. The form of tensor δ_{ijkl} resembles that of magnetostriction tensor [49]. We obtained the following expression for the free-energy in terms of the direction cosines $\alpha_i = M_i / M_0$:

$$G_{ME}^a = -\delta_{ijkl} E_i E_j \alpha_k \alpha_l . \tag{10}$$

Then, by comparing this expression with the uniaxial anisotropy term $G_o^a = -K_u \alpha_3^2$ (and taking into account the condition $\sum_i \alpha_i^2 = 1$) we find that the change in the uniaxial anisotropy constant is given by

$$\Delta K_u = \left(\delta_{ij33} - 1/2(\delta_{ij11} + \delta_{ij22})\right) E_i E_j = \left(\delta_{ij33} - 1/2(\delta_{ij11} + \delta_{ij22})\right) \rho_{im} \rho_{jn} j_m j_n . \tag{11}$$

Once again this contribution is anisotropic with respect to the electric field direction. However corresponding expressions are much more cumbersome than Eq.(8). In our case we have $\overline{E} = (0,0,E_3)$. Using the non-zero tensor coefficients we obtained the following expression for the change in the anisotropy constant:

$$\Delta K_u = (\delta_{3333} - \delta_{3311}) E_\parallel^2 = (\delta_{3333} - \delta_{3311}) \rho_\parallel^2 j_\parallel^2 . \tag{12}$$

After substituting for the parameters in Eq (12) we estimated $(\delta_{3333} - \delta_{3311})$= -2.97*10^{-2} $erg/(V^2 cm)$ or -2.67*10^3 (dimensionless) in CGS.

4. Conclusions

In conclusion, the first observation of room temperature current/electric field-induced nonlinear magnetoelectric effects in ferrimagnetic single crystal M-type hexaferrite is reported. It is shown that conduction current along the c-axis of the strontium hexaferrite platelet induces variations in the saturation magnetization and uniaxial anisotropy energy. Microwave measurement techniques have been used for estimation of changes in magnetic parameters from magnetostatic mode frequencies for the multidomain ($H_0 = 0$) and single domain resonances. The measured current-induced frequency shift amounted to ≈220 MHz in the multidomain state and ≈320 MHz in the saturated state for E ~ 1 kV/cm (I_{DC} = 70 mA). Changes in the magnetic parameters due to Joule heating were estimated to be negligible in comparison with the observed ME effects. The saturation magnetization is found to decrease and the uniaxial anisotropy field increases linearly with the applied electric power density (or E^2). A phenomenological description of the observed magneto-bielectric effects, consistent with intrinsic crystallo-magnetic symmetry of hexaferrite, has been proposed and the MBE coupling coefficients have been estimated from data on change in the magnetization and anisotropy field. The MBE effect is of technological importance for current tunable mm-wave ferrite devices such as resonators and filters for use in high frequency communication systems.

Acknowledgments

The samples used in this study were provided by Professor Balbashov, Moscow Power Engineering Institute, Moscow, Russia. The authors are grateful to B.A. Okhrimenko for valuable discussions. The research at Taras Shevchenko National University of Kyiv was partially supported by a grant from the Ministry of Education and Science of Ukraine (0115U000163). The research at Oakland University was partially supported by a grant from the NSF (ECCS- 1307714).

References

1. L. Berger, Phys. Rev. B **54**, 9353 (1996).
2. J.C. Slonczewski, JMMM **159**, L1 (1996).
3. A. Brataas, A.D. Kent, and H. Ohno, Nat. Materials **11**, 372 (2012).
4. D.C. Ralph, M.D. Stiles, JMMM **320,** 1190 (2008).
5. V. E. Demidov, S. Urazhdin, H. Ulrichs, V.Tiberkevich, A. Slavin, D. Baither, G. Schmit, and S. O. Demokritov, Nature Mater. **11**, 1028 (2012).
6. J.A. Katine, F.J. Albert, R.A. Buhrman, E.B. Myers, and D.C. Ralph, Phys. Rev. Lett. **84,** 3149 (2000).
7. W.H. Rippard, M.R. Pufall, S. Kaka, S.E. Russek, and T.J. Silva, Phys. Rev. Lett. **92**, 027201 (2004).
8. N. A. Spaldin and M. Fiebig, Science **309**, 391 (2005).
9. N. A. Spaldin, S. W. Cheong, and R. Ramesh, Physics Today, **63**, 38 (2010).
10. J. Ma, J. Hu, Z. Li, and C. W. Nan, Adv. Mater. **23**, 1062 (2011).
11. J. Zhai, Z. Xing, S. Dong, J. Li and D. Viehland, J. Am. Ceram. Soc., **91**, 351 (2008).
12. C.-W. Nan, M. I. Bichurin, S. Dong, D. Viehland, and G. Srinivasan, J. Appl. Phys. **103**, 031101 (2008).
13. J. Zhai, Z. Xing, S. Dong, J. Li and D. Viehland, Appl. Phys. Lett. **88**, 062510 (2006).
14. S. Priya, R. Bergs, and R. A. Islam, J. Appl. Phys. **101**, 024108 (2007).
15. G. Srinivasan, I.V. Zavislyak, and A.S. Tatarenko, Appl. Phys. Lett. **89**, 152508 (2006).
16. A.B. Ustinov and G. Srinivasan, Appl. Phys. Lett. **93**, 142503 (2008).
17. S. D. Bader and S. S. P. Parkin, Ann. Rev. of Condens. Matter Phys. **1**, 77 (2010).
18. H. Schmid, J. Phys.: Condens. Matter **20,** 434201 (2008).
19. W. Eerenstein, N. Mathur, and J. Scott, Nature **442**, 759 (2006).
20. D. Khomskii, Physics **2**, 20 (2009).
21. J.-P. Rivera, Eur. Phys. J. B **71**, 299 (2009).

22. A.P. Pyatakov, A.S. Sergeev, E.P. Nikolaeva, T.B. Kosykh, A.V. Nikolaev, K.A. Zvezdin, and A.K. Zvezdin, Phys. Usp. **58,** 1077 (2015).

23. Y.-Y. Song, J. Das, P. Krivosik, N. Mo, and C. E. Patton, Appl. Phys. Lett. **94**, 182505 (2009).

24. O. V. Prokopenko, I. N. Krivorotov, E. N. Bankowski, T. J. Meitzler, V. S. Tiberkevich, and A. N. Slavin, Journal of Applied Physics **114**, 173904 (2013).

25. H. Murakawa, Y. Onose, and Y.Tokura, Phys. Rev. Lett. **103**, 147201 (2009).

26. H. Izadkhah, S. Zare, S. Somu, and C. Vittoria, Appl. Phys. Lett. **106**, 142905 (2015)

27. M. Mohebbi, K. Ebnabbasi, and C.Vittoria, J. Appl. Phys. **113**, 17C710, 2013.

28. K. Okumura, K. Haruki, T. Ishikura, S. Hirose, and T. Kimura, Appl. Phys. Lett. **103**, 032906 (2013).

29. S. Hirose, K. Haruki, A. Ando, and T. Kimura, Appl. Phys. Lett. **104**, 022907 (2014).

30. G. Aubert, J. Appl. Phys. **53**, 8125 (1982).

31. C.M. Fang, F. Kools, R. Metselaar, G. deWith, and R. A. de Groot, J. Phys.: Condens. Matter **15,** 6229 (2003).

32. K. Zaveta, Phys. Stat. Sol. **3**, 2111 (1963).

33 F.-C. Chiu, Advances in Materials Science and Engineering, **2014**, 578168 (2014).

34. F. J. Rachford, P. Lubitz, and C. Vittoria, J. Appl. Phys. **53**, 8940 (1982).

35. D. J. De Bitetto, J. Appl. Phys. **35**, 3482 (1964).

36. D. Polder, and J. Smit, Reviews of Modern Physics, **25**, 89 (1953).

37. R. E. Greenwood and G. P. Rodrigue, J. Appl. Phys. **38**, 1401 (1967).

38. M. A. Popov, I. V. Zavislyak, A. S. Tatarenko, G. Srinivasan, and A. M. Balbashov, IEEE Trans. on Mag. **45**, 2053 (2009).

39. M. Beleggia, M. De Graef, and Y. T. Millev, J. Phys. D: Appl. Phys. **39,** 891 (2006).

40. T. Yukawa, J. Ikenoue, S. Yamada, and K. Abe, J. Appl. Phys. **49**, 376 (1978).

41. K.-H. Hellewege and A. M. Hellewege ed., *Landolt-Börnstein, New Series III/4b, Ch. 7.6* (Springer-Verlag, New York, 1970).

42. B. T. Shirk and W. R. Buessem, J. Appl. Phys. **40**, 1294 (1969).

43. H. G. Richter, H. E. Dietrich, IEEE Trans. Mag. **MAG-4**, 263 (1968).

44. J. O. Artman, Phys. Rev. **105**, 62 (1957).

45. A.G. Gurevich, G.A. Melkov, *Magnetization Oscillations and Waves* (CRC Press, New York, 1996).

46. J. R. Truedson, K. D. McKinstry, P. Kabos, and C. E. Patton, J. Appl. Phys. **74**, 2705 (1993).

47. R. C. Pullar, Progress in Materials Science, **57,** 1191 (2012).

48. Y. Xu, G. L. Yang, D.P. Chu, and H.R. Zhai, JMMM **31-34**, 815 (1983).

49. R. E. Newnham, *Properties of Materials: Anisotropy, Symmetry, Structure* (Oxford University Press, Oxford, 2005).

50. International Tables for Crystallography, Volume D: Physical properties of crystals, Second edition (2013), ISBN: 978-1-118-76229-5 Edited by A. Authier, p.133.